NASA TM X-1400

HEAT-TRANSFER MEASUREMENTS ON A LOW-FINENESS-RATIO CYLINDER AT A MACH NUMBER OF 10.4 AND ANGLES OF ATTACK FROM 0° TO 90°

By Philip E. Everhart

Langley Research Center
Langley Station, Hampton, Va.

NATIONAL AERONAUTICS AND SPACE ADMINISTRATION

For sale by the Clearinghouse for Federal Scientific and Technical Information
Springfield, Virginia 22151 – CFSTI price $3.00

HEAT-TRANSFER MEASUREMENTS ON A LOW-FINENESS-RATIO CYLINDER AT A MACH NUMBER OF 10.4 AND ANGLES OF ATTACK FROM 0° TO 90°

By Philip E. Everhart
Langley Research Center

SUMMARY

Measurements of aerodynamic heat transfer have been made on the Nimbus B fuel capsule at a free-stream Mach number of 10.4. The fineness-ratio-2 cylinder was tested at angles of attack from 0° to 90° for Reynolds numbers, based on free-stream conditions and cylinder diameter, from 0.17×10^6 to 0.40×10^6. The results indicate that end effects are primarily concentrated within 1/2 diameter of the ends of the cylinder for the angles of attack of this investigation. When the face of the cylinder was normal to the flow, its heating was less than that calculated for a flat face. The heating on the recessed face was a maximum at angles of attack from 40° to 50° where the local inflection in the bow shock evidenced significant changes in the flow pattern over the face of the cylinder.

INTRODUCTION

Experimental and theoretical heat-transfer studies of cylinders generally have been concerned with the effects of yaw angle on the heat transfer on a cylinder of infinite length. Published information on heat transfer on the ends of a cylinder is limited to the condition of the circular face normal to the flow. (For example, see ref. 1.) In the present investigation, convective heating rates have been measured on a very short cylinder (length equal to 2 diameters) over a wide range of model attitudes. Heat-transfer measurements on the end of the cylinder as well as along the side walls are presented.

The model representing the fuel capsule of the Nimbus B weather satellite was tested in the Langley continuous-flow hypersonic tunnel at a nominal Mach number of 10.4 and angles of attack from 0° to 90°. The Reynolds numbers, based on free-stream conditions and cylinder diameter, ranged from 0.17×10^6 to 0.40×10^6. Heat-transfer data were obtained by means of a transient calorimeter method. Pressure distributions, as well as force data, were obtained in other test programs; however, data pertinent to the present study have been used wherever necessary.

SYMBOLS

The units used for the physical quantities defined in this paper are given both in U.S. Customary Units and in the International System of Units (SI). Factors relating these two systems of units are presented in reference 2.

c_p specific heat of air at constant pressure

c_w specific heat of model skin material

D diameter of cylinder

h aerodynamic heat-transfer coefficient

L length of cylinder

M_∞ free-stream Mach number

$N_{St,\infty}$ Stanton number based on free-stream conditions, $\frac{q}{T_{aw} - T_w} \Big/ \rho_\infty u_\infty c_p$

q heat-transfer rate

$R_{\infty,D}$ Reynolds number based on cylinder diameter and free-stream conditions

s distance from center of face of cylinder (see fig. 4)

T_{aw} adiabatic wall temperature

T_t free-stream stagnation temperature

T_w temperature of the wall

u_∞ free-stream velocity

x distance aft from forward edge of cylinder

α angle of attack measured in plane of axial center line of model

ρ_∞ free-stream density

ρ_w density of skin material

τ_w model skin thickness

ϕ radial angle about body axis (see fig. 4)

APPARATUS AND TESTS

Tunnel

The heat-transfer tests were conducted in the Langley continuous-flow hypersonic tunnel at a nominal Mach number of 10.4. A photograph of the facility is shown in figure 1(a). The test air is heated by an electrical-resistance-tube heater to avoid liquefaction when expanded through a contoured, three-dimensional, water-cooled nozzle to test conditions in a 78.7-cm-square (31-inch) test section. A schematic diagram of the facility is shown in figure 1(b). Starting as a blowdown tunnel using bottled air and a vacuum sphere and transferring to the compressor circuit as the area of the second minimum is reduced, the tunnel is capable of continuous operation on the closed loop.

Model

A photograph of the model mounted for testing is presented in figure 2 and details of the recessed face of the model are shown in figure 3. The model, 7.582 cm (2.985 inches) in diameter, was constructed of inconel with a wall thickness of 0.079 cm (0.031 inch). Detailed model dimensions and thermocouple locations are shown in figure 4. Chromel-alumel thermocouples (28-gage wire) were installed by drilling holes in the cylinder surface with the leads extending through the skin; the holes were then welded closed with an inconel welding rod and the exterior surface polished. The lip at the juncture of the cylinder and face was formed from two 0.079-cm-thick (0.031-inch) plates welded together (fig. 4) with the thermocouples at $s/D = 0.488$ embedded within this joint. The reference juncture of all thermocouples was maintained at a temperature of 325° K (585° R).

Tests

The tests were conducted at a nominal free-stream Mach number of 10.4, an average stagnation temperature of 981° K (1766° R), and angles of attack from 0° (face normal to flow) to 90° (cylinder normal to flow). The tunnel stagnation pressure was varied from 33 to 80 atmospheres and the corresponding free-stream Reynolds numbers, based on cylinder diameter, ranged from 0.17×10^6 to 0.40×10^6. Details of the test conditions are given in table I.

Heat-transfer data were obtained by means of a transient calorimeter method injecting the model through one of the window openings (fig. 5) into the test section. With the tunnel operating at the desired test conditions, a vertical door, which covered the test-section opening, was retracted and the model, which was oriented at the desired angle of attack, was injected into the flow. The time from the moment the model was first exposed to the flow until it reached the center line of the test section was approximately 1/4 second. Data recording began with the start of model insertion and continued for 5 seconds after the model reached the center of the tunnel. The temperature-time data and tunnel-flow conditions were automatically recorded on magnetic tape by an analog-to-digital converter at 0.05-second intervals. After the temperature-time history was recorded, the model was retracted and cooled to approximately room temperature before the succeeding run.

The convective heat-transfer coefficient, defined in terms of the heat input to the model, was calculated from the temperature-time histories at the thermocouple locations by using the following equation:

$$q = h\left(T_{aw} - T_w\right) = \rho_w c_w \tau_w \frac{dT_w}{dt}$$

The temperature-time derivative $\frac{dT_w}{dt}$ was obtained by fitting a quadratic least-square curve to the measured data and then differentiating this curve. The measured values of skin thickness were used in the calculations. A skin-density value of 8248.61 kg/m^3 (514.94 lb/ft^3) was used. Values of specific heat were obtained from the following empirical equation derived from the data of reference 3:

$$c_w = 0.0810 + 0.0000756T_w$$

where T_w is in degrees Kelvin.

Values of adiabatic wall temperature T_{aw} equal to the free-stream stagnation temperature T_t were used in the calculations. Real-gas properties were used in calculating stream conditions. The data are presented without conduction corrections.

RESULTS AND DISCUSSION

Shadowgraphs

Figure 6 presents shadowgraphs obtained from the force test of the cylinder model at varying angles of attack. For this phase of the investigation, different models were used and the models were not injected but mounted on a strut attached to the ceiling of the

tunnel. The sting was attached to the base of the cylinder for angles of attack up to 35°; whereas, at higher angles of attack, it was attached to the center of the cylinder. The bow shock was detached and symmetrical at an angle of attack of 0° for the recessed face of the cylinder. (See fig. 6(a).) At an angle of attack of 35°, the shock standoff distance was relatively small at the forward edge of the cylinder and over the recessed face inasmuch as air flowing into this shallow cavity exits from it forcing the shock farther from the face of the model. The distance from the face-side juncture to the inflection point increased with angle of attack up to 65°. (See fig. 6(a).) At higher angles of attack the inflection point disappeared and the shock was symmetrical about the cylinder side at an angle of attack of 90°.

Shadowgraphs of the cylinder with a flat face are presented in figure 6(b). No inflection point can be seen. At an angle of attack of 90°, the shock shape for the two faces is similar.

Heat Transfer

The measured heat-transfer data are presented in figure 7 in terms of Stanton number and Reynolds number $\left(N_{St,\infty}\sqrt{R_{\infty,D}}\right)$ as a function of the nondimensional distance from the center of the face of the cylinder (s/D) for angles of attack from 0° to 90°. The juncture of the face and side of the cylinder is located at $s/D = 0.5$. The model was instrumented so that the thermocouples on the face were 3.5° out of line with the thermocouples on the cylinder side. (See fig. 4.) In presenting the data, this offset in the radial angle is neglected and radial angles of $\phi = 0^{\circ}$, 30°, 60°, 90°, 135°, and 180° are used. The $\phi = 0^{\circ}$ ray is the windward ray and the $\phi = 180^{\circ}$ is the leeward ray.

The spread in the heating on the face of the cylinder for most of the test angles of attack is probably due to the steps on the cylinder face. (See fig. 7.) The heating on the cylinder face is discussed in more detail subsequently. On the side of the cylinder, an expansion of the flow over the rim of the cylinder at low angles of attack (figs. 7(a) and 7(b)) produces a minimum in the heating. On the 90° ray, the expansion occurs for angles of attack up to 32.5°. Following this expansion region, the heating parameter increases slightly and then decreases in the streamwise direction. This decrease continues for angles of attack up to 50°. At the higher angles of attack, a substantial rise in the windward heating ($\phi = 0^{\circ}$) occurs at the rearmost edge of the cylinder. The distribution on the side of the cylinder should be symmetrical at an angle of attack of 90° (fig. 7(j)).

The heating in the base region was calculated using a skin thickness of 0.079 cm (0.031 inch); however, the construction of the model was such that the skin thickness at the face-cylinder juncture could more properly be considered twice this value. (See

fig. 4.) The effect of this additional material would be to decrease the indicated heating rate for the thermocouples at $s/D = 0.488$. The adjacent thermocouples at $s/D = 0.532$ are also likely affected by the increased material at the lip. If the effect of conduction had been properly accounted for, the heating would have been symmetrical at an angle of attack of 90°.

The data for the cylinder at an angle of attack of 90° (fig. 7(j)) are compared with predicted values obtained from the Fay and Riddell equation (ref. 4). Except for the regions less than 1/2 diameter from the cylinder ends, good agreement is shown between the predicted values and the measured values for the windward ray ($\phi = 0^{\circ}$). On the portion of the cylinder end away from the sting ($0.5 < s/D < 1.0$), the $\phi = 0^{\circ}$ data show little effect of the proximity of the end, as evidenced by the small difference (less than 15 percent) between the cylinder theory and the data. On the portion of the cylinder end near the sting, strong end effects are seen on all the peripheral stations around the cylinder.

To facilitate the interpretation of the heating to the face of the cylinder, the heat-transfer parameter $N_{St,\infty}\sqrt{R_{\infty,D}}$ presented in figure 7 is shown again in the form of contour plots in figure 8. The irregular distribution in the heat-transfer data on the face of the cylinder at an angle of attack of approximately 0° is probably due to the steps on the face of the cylinder. (See sketch in fig. 7(a).) The heating is not entirely symmetrical at an angle of attack of 0° as might be expected where the center of the disk is recessed. (See figs. 7(a) and 8(a).) As the angle of attack was increased, the shape of the distribution on the $\phi = 0^{\circ}$ ray suggests that the flow separates just behind the rim and produces the lower heating at the $s/D = 0.28$ station. The level of the heating on the face of the cylinder increased slightly with angles of attack from 0° to 25° and reached a maximum at about an angle of attack of 50° where the flow field apparently changes, as evidenced by the inflection in the bow shock. At higher angles of attack, the heat transfer on the face of the cylinder decreased.

The highest heating occurred at the juncture of the face and side of the cylinder ($s/D = 0.5$) at angles of attack of 40° to 50°. The thermocouples at $s/D = 0.49$ and 0.53 are not truly indicative of the local heat transfer because the heat flow rates in the skin are not one-dimensional as assumed in the data reduction and are heavily affected by conduction, yet the trends they produce are believable. Approximately equal heating rates were obtained at the foremost edge of the lip ($\phi = 0^{\circ}$) and the rearmost edge ($\phi = 180^{\circ}$). The high heating at $\phi = 0^{\circ}$ was expected because the stagnation point is located here. The high heating on the lip at $\phi = 180^{\circ}$ is associated with the formation of a shock approximately normal to the surface at this angle of attack. (See fig. 6(b).)

According to reference 4, the heat transfer on a flat-face disk normal to the flow is 0.56 of that on a hemisphere of the same radii. The value of $N_{St,\infty}\sqrt{R_{\infty,D}}$ thus obtained is compared with the measured data at the center of the face at an angle of attack of 0°. (See fig. 7(a).) The measured value is lower than the theoretical value due to the recessed face.

Measured data (not shown) indicated that the Stanton number on the cylinder was invariant with Reynolds number. However, for most of the angles of attack, an increase in $N_{St,\infty}\sqrt{R_{\infty,D}}$ with unit Reynolds number is present on the face of the cylinder. (See fig. 9.) The variation of the data with surface distance is essentially the same for all Reynolds numbers.

CONCLUSIONS

Measurements of aerodynamic heat transfer have been made on a low-fineness-ratio cylinder at a free-stream Mach number of 10.4. The fineness-ratio-2 cylinder was tested at angles of attack from 0° to 90° for Reynolds numbers, based on free-stream conditions and cylinder diameter, from 0.17×10^6 to 0.40×10^6. The results indicate that end effects are primarily concentrated within 1/2 diameter of the ends of the cylinder for the angles of attack of this investigation. When the face of the cylinder was normal to the flow, its heating was less than that calculated for a flat face. The heating on the recessed face was a maximum at angles of attack from 40° to 50° where the local inflection in the bow shock evidenced significant changes in the flow pattern over the face of the cylinder.

Langley Research Center,
National Aeronautics and Space Administration,
Langley Station, Hampton, Va., February 24, 1967,
124-07-01-39-23.

REFERENCES

1. Stoney, William E., Jr.; and Markley, J. Thomas: Heat-Transfer and Pressure Measurements on Flat-Faced Cylinders at a Mach Number of 2. NACA TN 4300, 1958.

2. Mechtly, E. A.: The International System of Units – Physical Constants and Conversion Factors. NASA SP-7012, 1964.

3. Lucks, C. F.; and Deem, H. W.: Thermal Properties of Thirteen Metals. Spec. Tech. Publ. No. 227, Am. Soc. Testing Mater., 1958.

4. Bertram, Mitchel H.; and Everhart, Philip E.: An Experimental Study of the Pressure and Heat-Transfer Distribution on a 70° Sweep Slab Delta Wing in Hypersonic Flow. NASA TR R-153, 1963.

TABLE I.- TEST CONDITIONS

Angle of attack, deg	Stagnation temperature		Stagnation pressure		Reynolds number, $R_{\infty,D}$	Mach number, M_∞
	^oK	^oR	kN/m^2	lb/in^2 abs		
0	991	1783	83.1	1205	39.30×10^4	10.46
7.5	977	1758	83.2	1207	40.47	10.46
15.0	976	1756	83.2	1207	40.55	10.46
25.0	978	1761	83.2	1206	40.30	10.46
32.5	982	1767	82.9	1203	39.92	10.46
40.0	979	1762	83.2	1207	40.27	10.46
50.0	1001	1801	83.0	1204	38.46	10.46
65.0	992	1786	82.7	1200	39.01	10.46
80.0	954	1717	69.2	1004	35.33	10.44
90.0	968	1743	69.4	1006	34.35	10.44
0	995	1791	52.1	755	24.58	10.40
7.5	977	1758	52.1	756	25.53	10.40
15.0	976	1757	52.1	756	25.56	10.40
25.0	970	1746	52.1	756	25.88	10.40
32.5	991	1783	52.1	755	24.81	10.40
40.0	992	1785	52.1	756	24.75	10.40
50.0	978	1761	51.9	753	25.31	10.40
65.0	978	1761	52.0	754	25.35	10.40
80.0	912	1641	54.7	794	30.70	10.40
90.0	1011	1820	52.9	767	24.18	10.40
0	986	1775	34.5	501	16.78	10.33
7.5	986	1775	34.5	501	16.78	10.33
15.0	985	1773	34.5	501	16.82	10.33
25.0	985	1773	34.5	500	16.80	10.33
32.5	988	1779	34.5	501	16.71	10.33
40.0	948	1707	34.3	497	17.98	10.33
50.0	997	1795	34.7	503	16.19	10.40
65.0	983	1770	34.0	493	16.61	10.33
80.0	1002	1803	35.9	520	16.84	10.34
90.0	978	1761	36.7	532	18.04	10.34

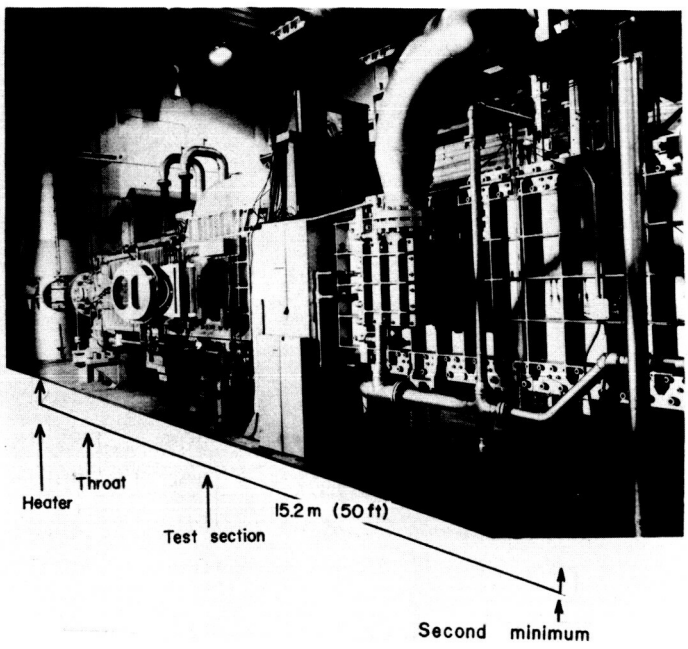

(a) General view. L-65-5822.1

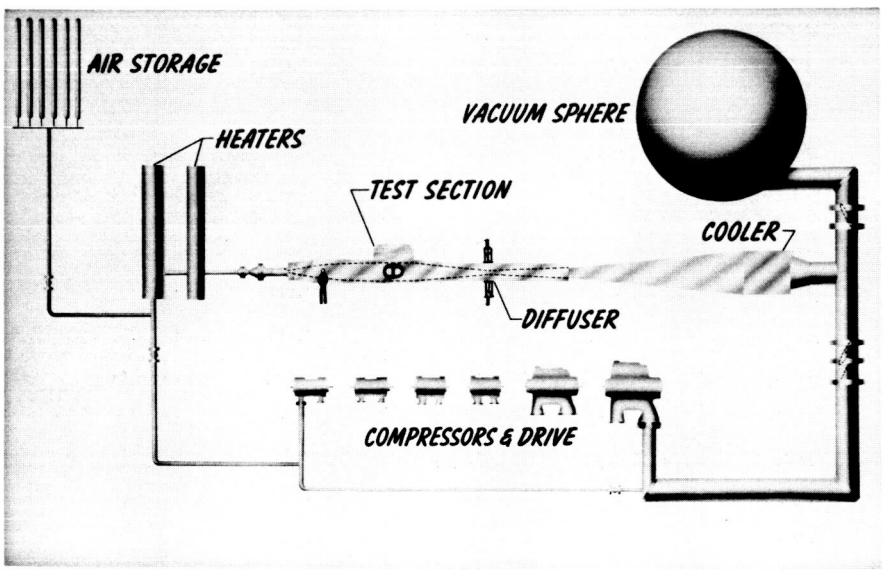

(b) Schematic diagram of the facility. L-67-956

Figure 1.- Langley continuous-flow hypersonic tunnel.

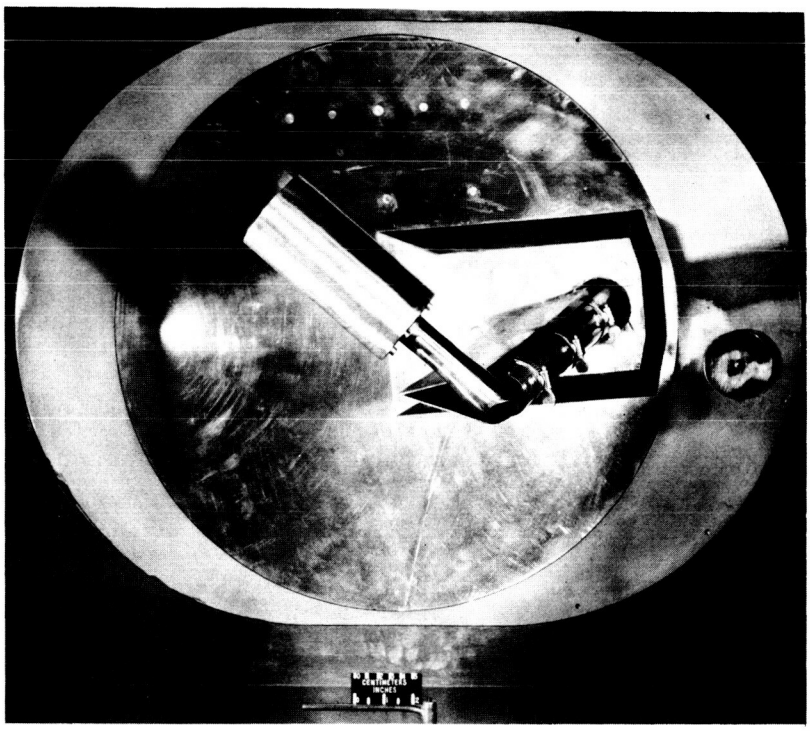

Figure 2.- Photograph of the model with modified strut. L-66-5693

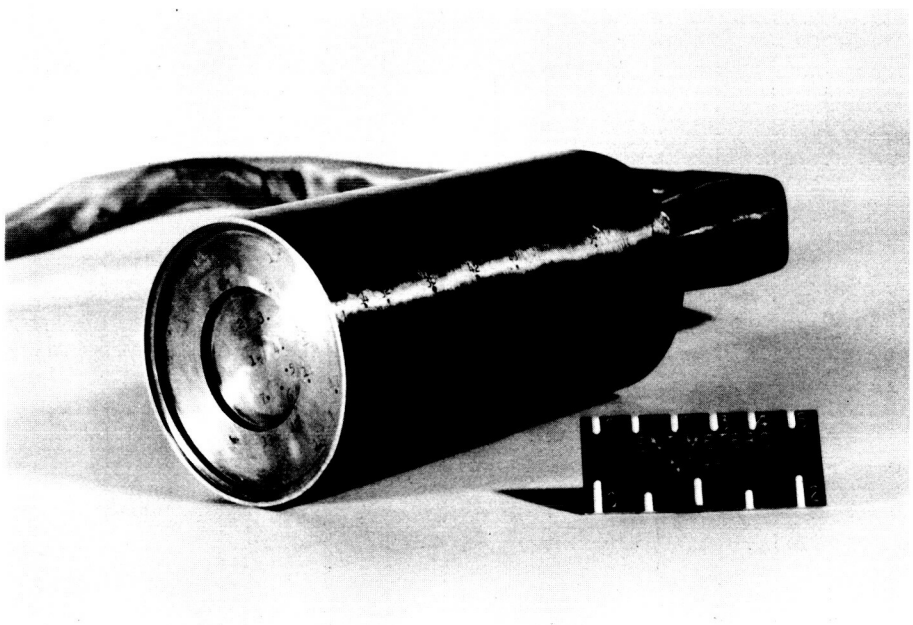

Figure 3.- Photograph of the Nimbus B fuel capsule model. L-66-6423

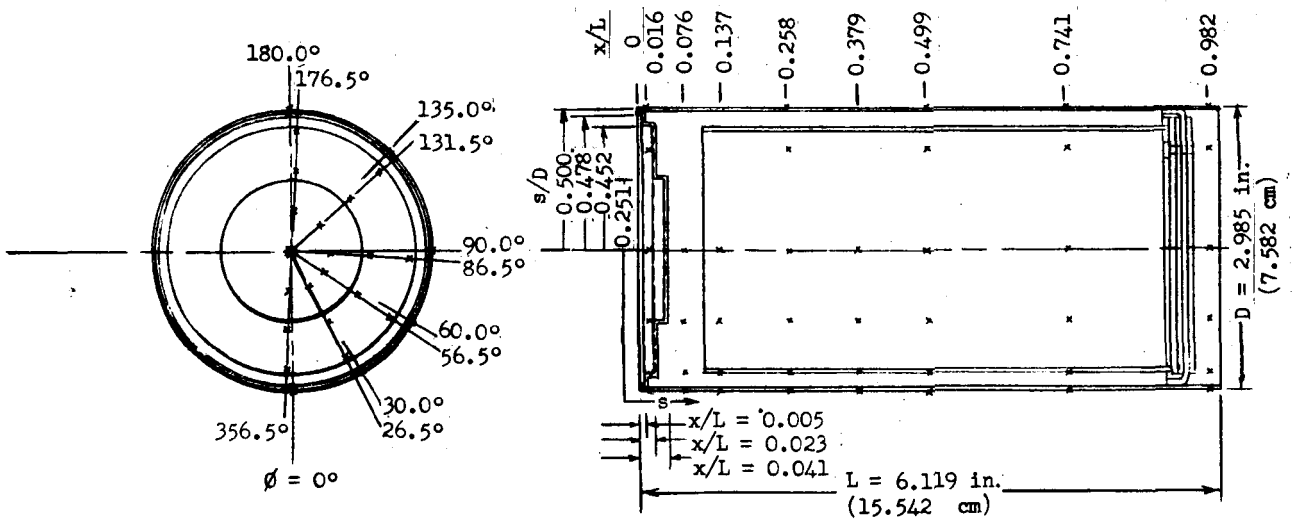

ø, deg	s/D	x/L	ø, deg	s/D	x/L	ø, deg	s/D	x/L
0	0	0.041	0	0.532	0.016	0	1.523	0.499
26.5	.141	↓	30.0	↓	↓	30.0	↓	↓
56.5	↓	↓	60.0	↓	↓	60.0	↓	↓
86.5	↓	↓	90.0	↓	↓	90.0	↓	↓
131.5	↓	↓	135.0	↓	↓	135.0	↓	↓
176.5	↓	↓	180.0	↓	↓	180.0	↓	↓
356.5	↓	↓	0	.656	.076	0	2.019	.741
26.5	.281	.023	30.0	↓	↓	30.0	↓	↓
56.5	↓	↓	60.0	↓	↓	60.0	↓	↓
86.5	↓	↓	90.0	↓	↓	90.0	↓	↓
131.5	↓	↓	0	.780	.137	135.0	↓	↓
176.5	↓	↓	30.0	↓	↓	180.0	↓	↓
356.5	↓	↓	60.0	↓	↓	0	2.514	.982
26.5	.422	↓	90.0	↓	↓	30.0	↓	↓
56.5	↓	↓	0	1.028	.258	60.0	↓	↓
86.5	↓	↓	30.0	↓	↓	90.0	↓	↓
131.5	↓	↓	60.0	↓	↓	135.0	↓	↓
176.5	↓	↓	90.0	↓	↓	180.0	↓	↓
356.5	↓	↓	135.0	↓	↓			
26.5	.488	0	180.0	↓	↓			
56.5	↓	↓	0	1.276	.379			
86.5	↓	↓	30.0	↓	↓			
131.5	↓	↓	60.0	↓	↓			
176.5	↓	↓	90.0	↓	↓			
356.5	↓	↓						

Figure 4.- Model dimensions and thermocouple locations.

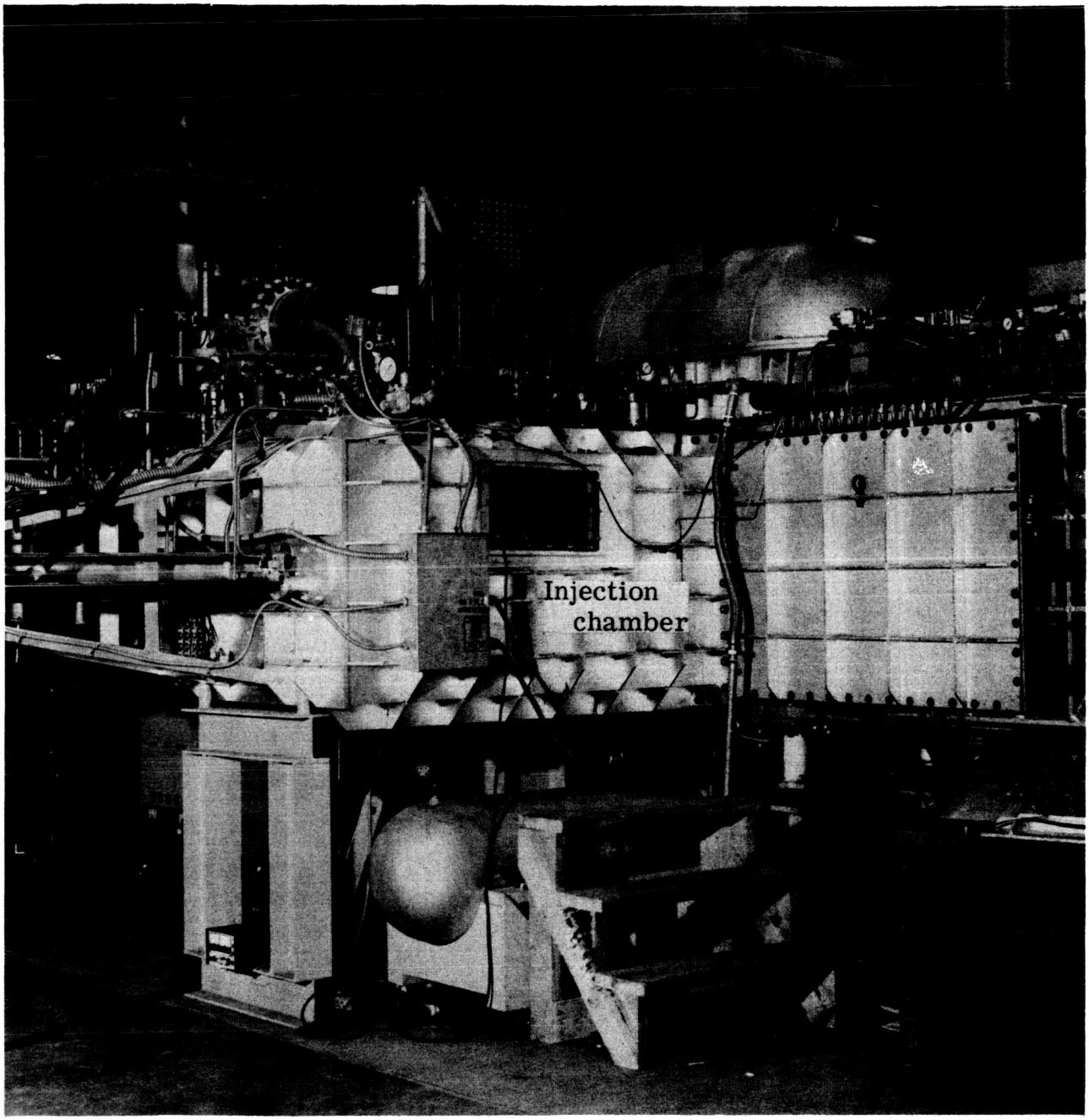

Figure 5.- Photograph of the injection chamber. L-65-5825

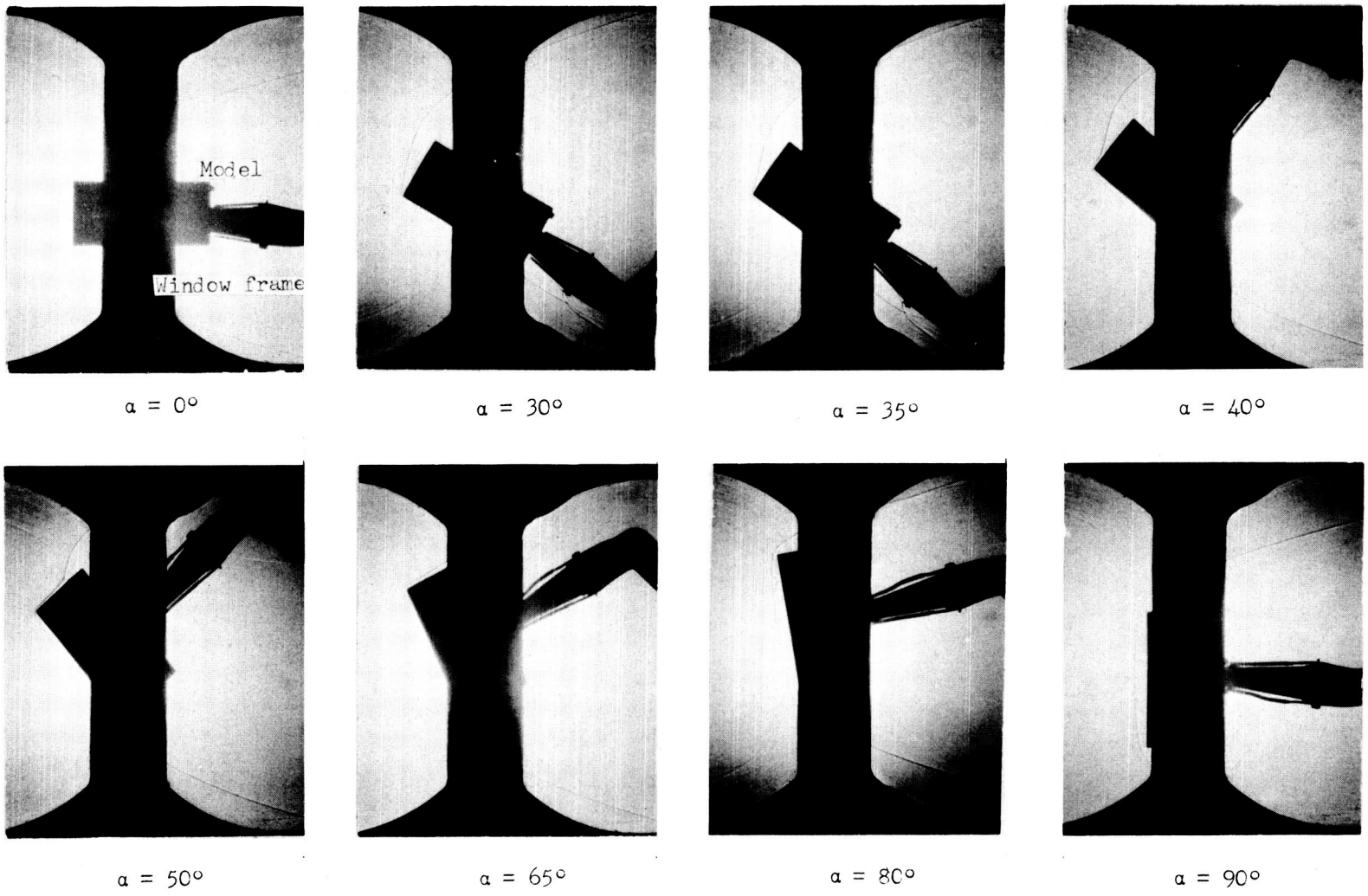

(a) Recessed face.

L-67-957

Figure 6.- Shadowgraphs of the Nimbus B fuel capsule model. $R_{\infty,D} = 39.79 \times 10^4$.

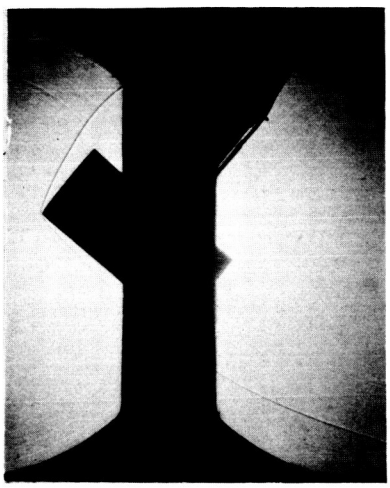

$\alpha = 40°$

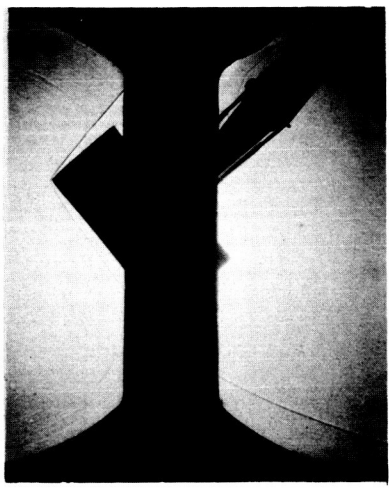

$\alpha = 50°$

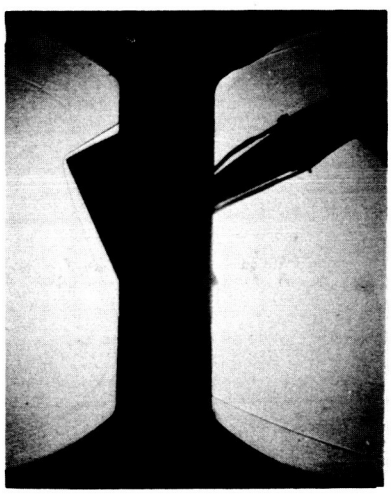

$\alpha = 65°$

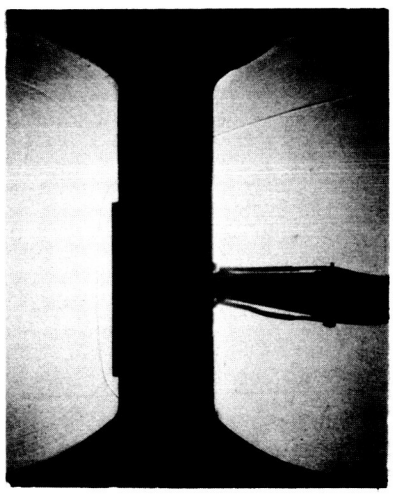

$\alpha = 90°$

(b) Flat face. L-67-958

Figure 6.- Concluded.

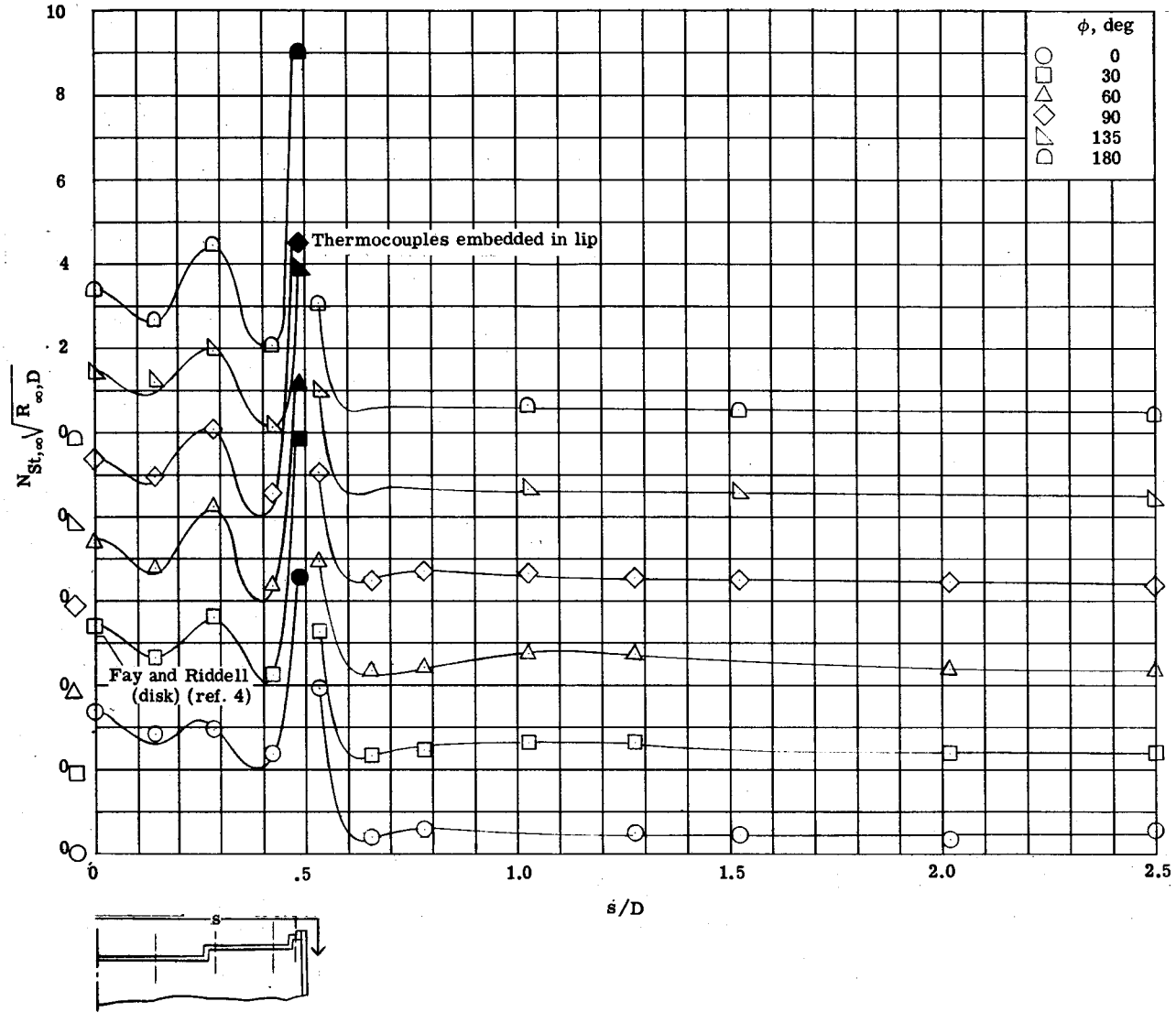

(a) $\alpha = 0^{0}$.

Figure 7.- Variation of heat-transfer parameter with distance s/D. $R_{\infty,D} = 39.79 \times 10^{4}$.

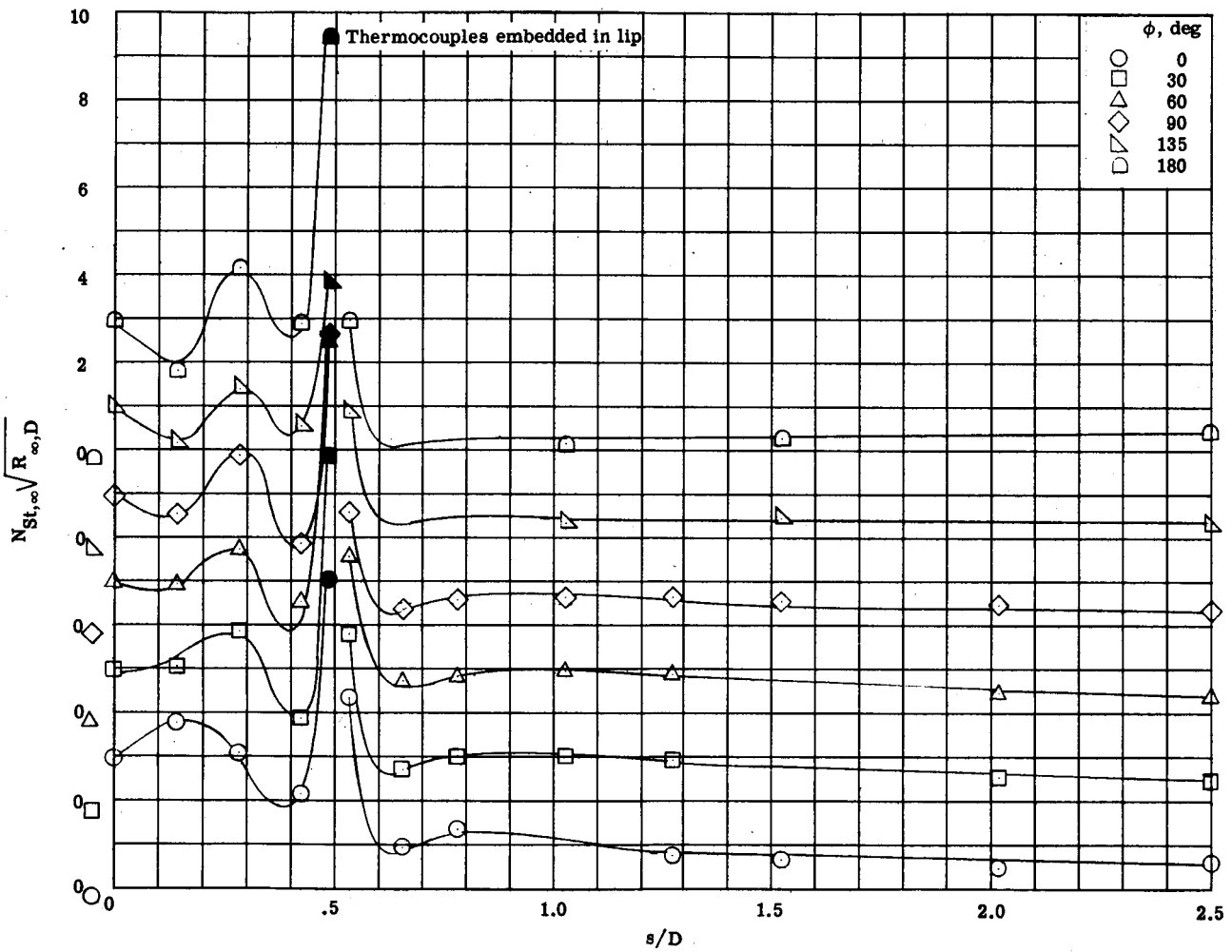

(b) $\alpha = 7.5^0$.

Figure 7.- Continued.

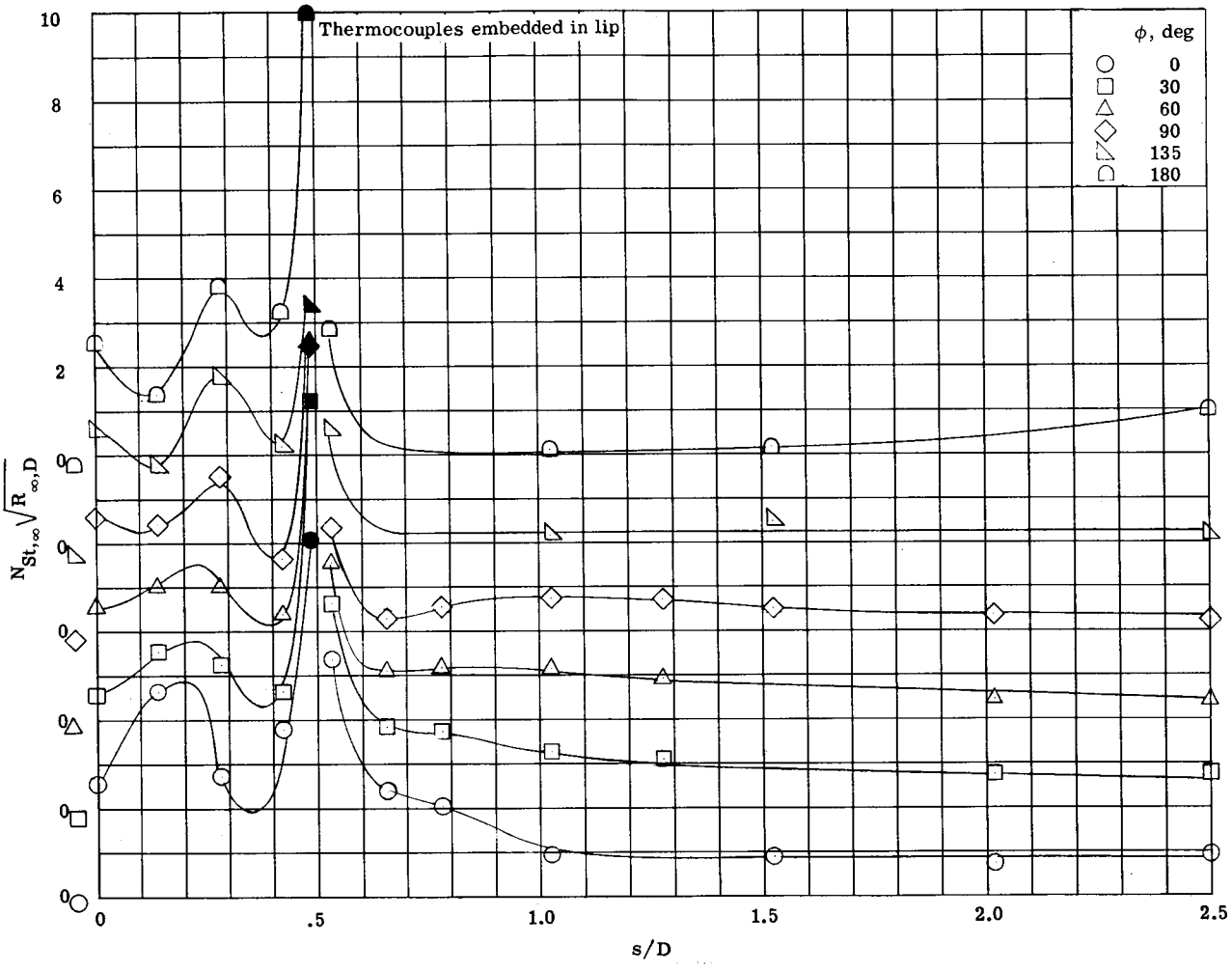

(c) $\alpha = 15.0^0$.

Figure 7.- Continued.

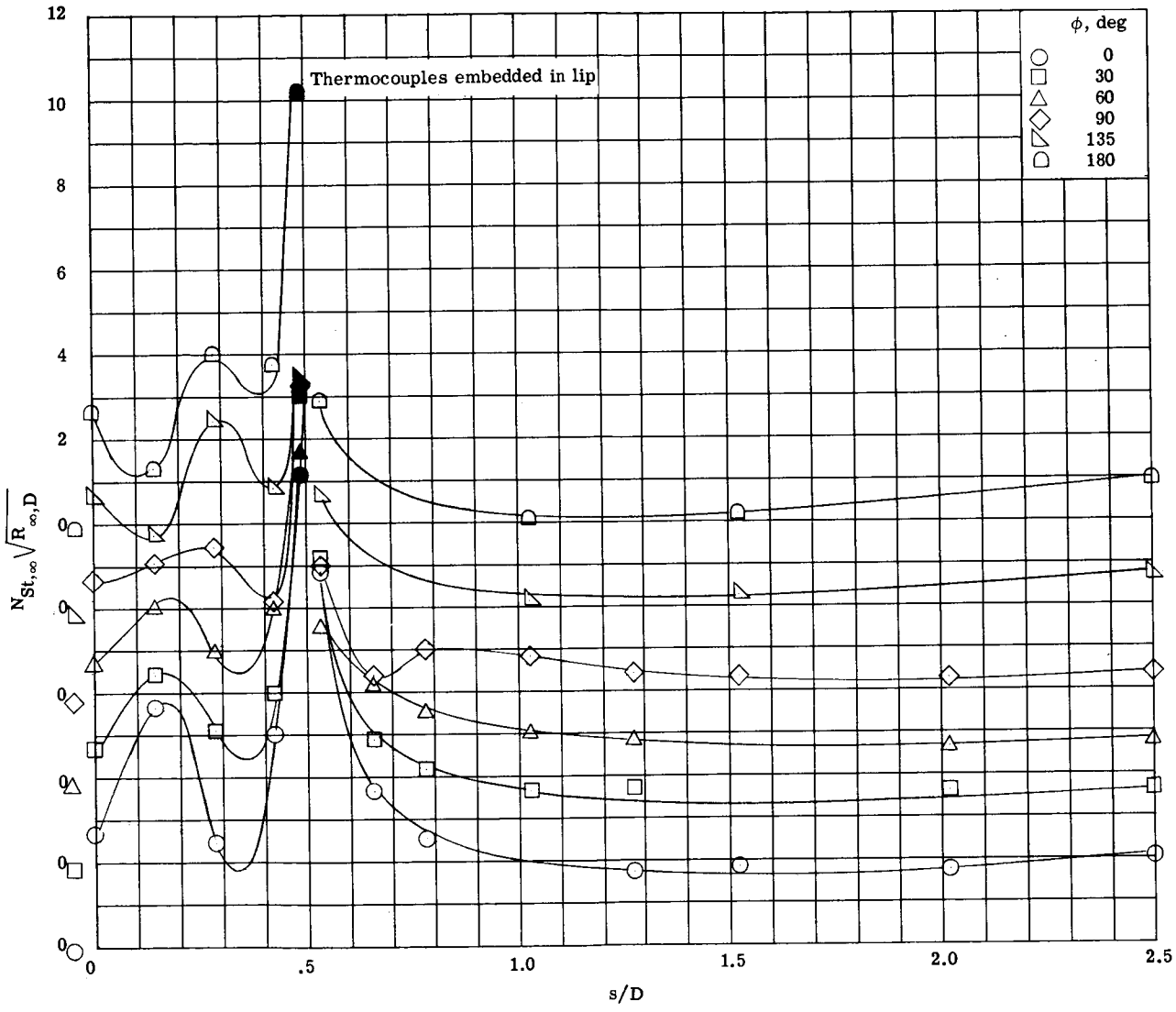

(d) $\alpha = 25.0^0$.

Figure 7.- Continued.

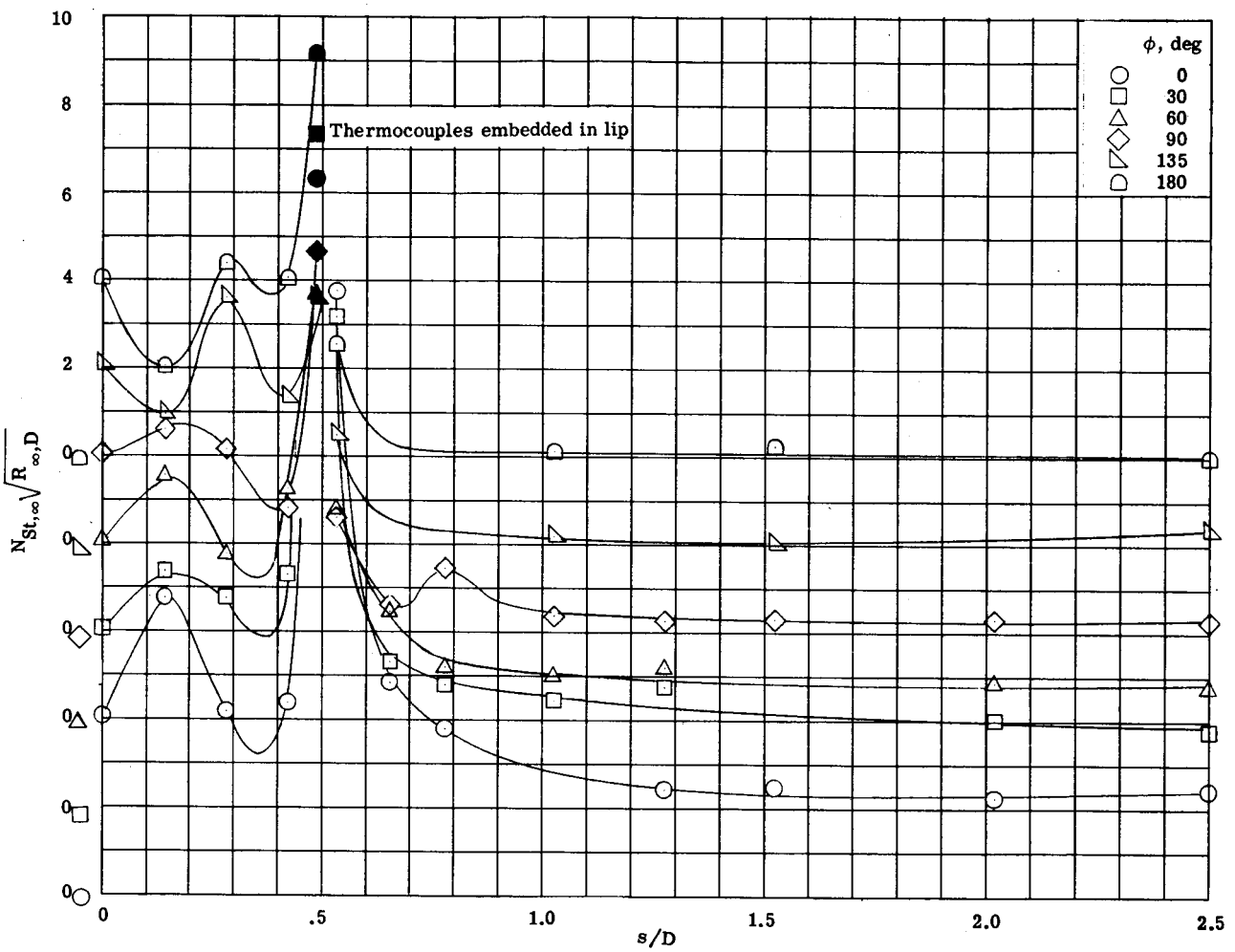

(e) $\alpha = 32.5^{0}$.

Figure 7.- Continued.

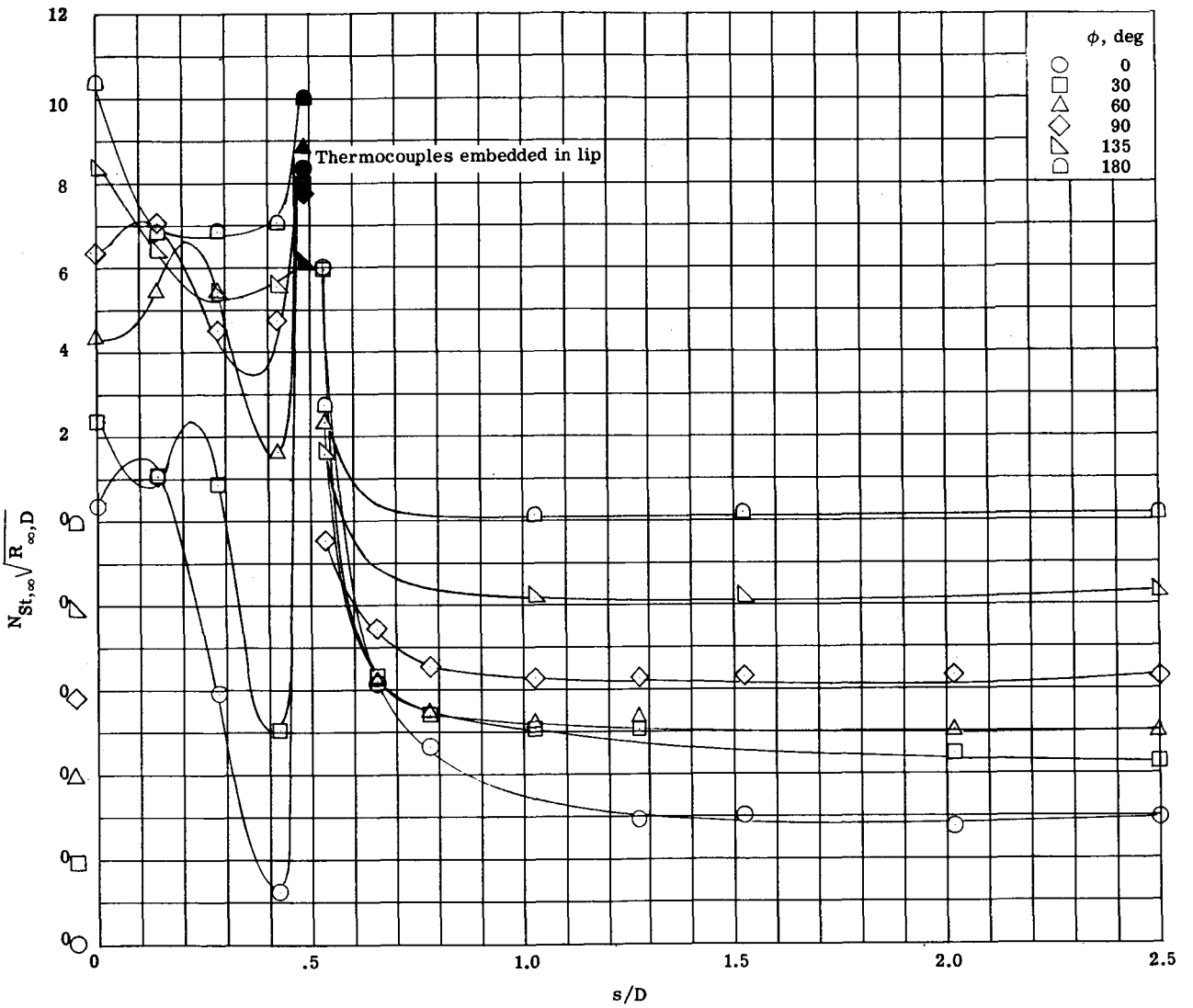

(f) $\alpha = 40.0^{0}$.

Figure 7.- Continued.

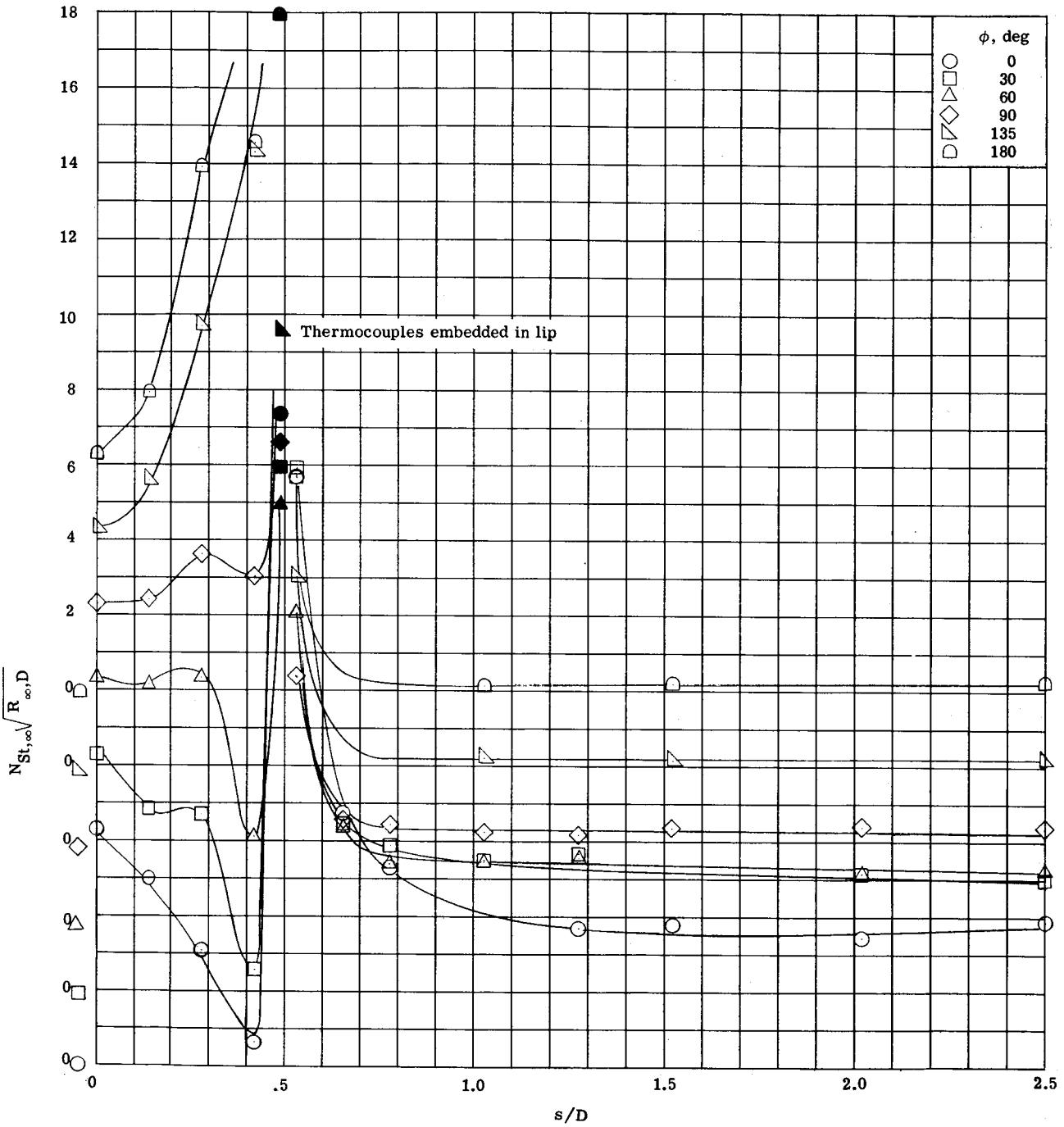

(g) $\alpha = 50.0^{o}$.

Figure 7.- Continued.

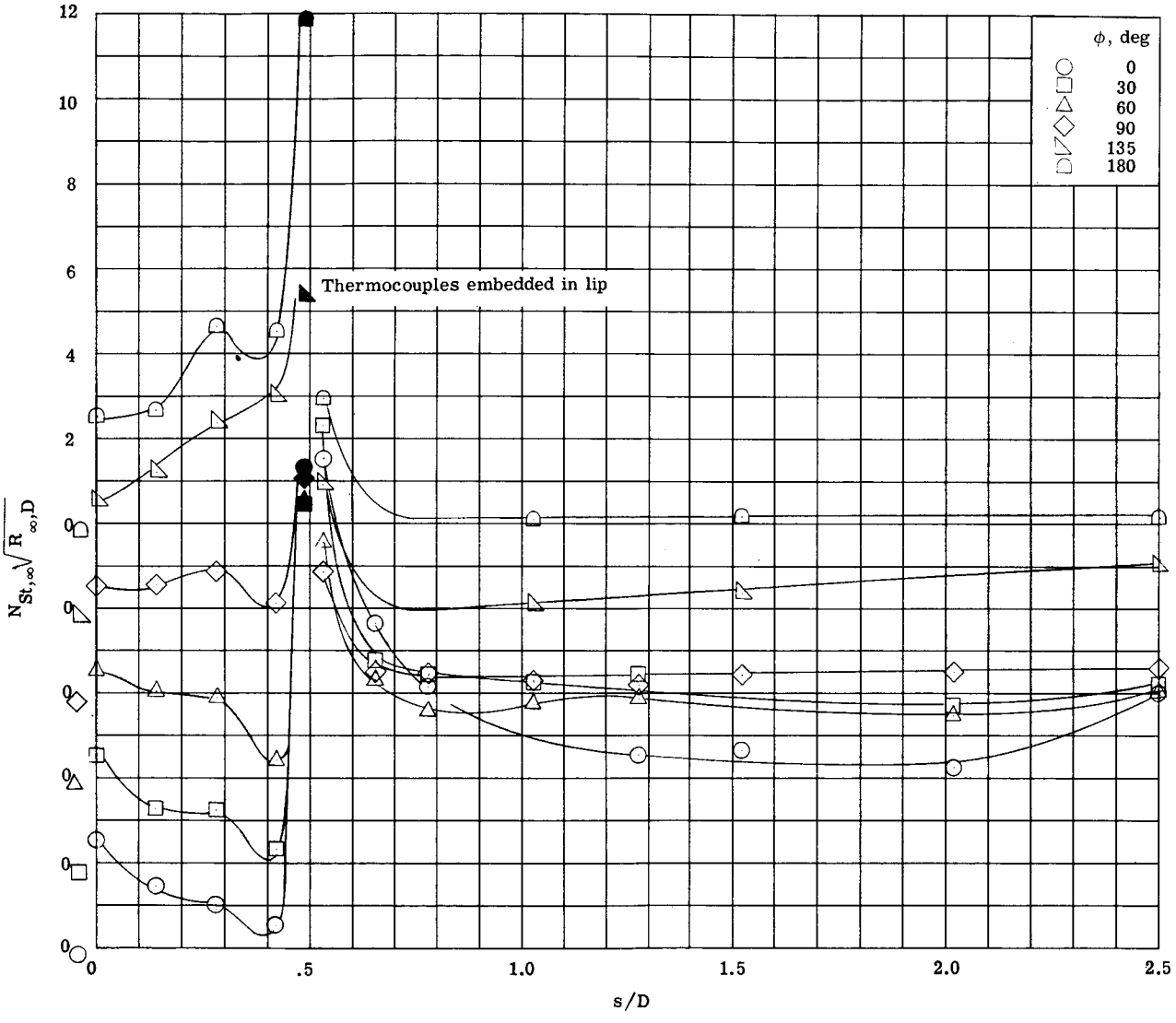

(h) $\alpha = 65.0^{0}$.

Figure 7.- Continued.

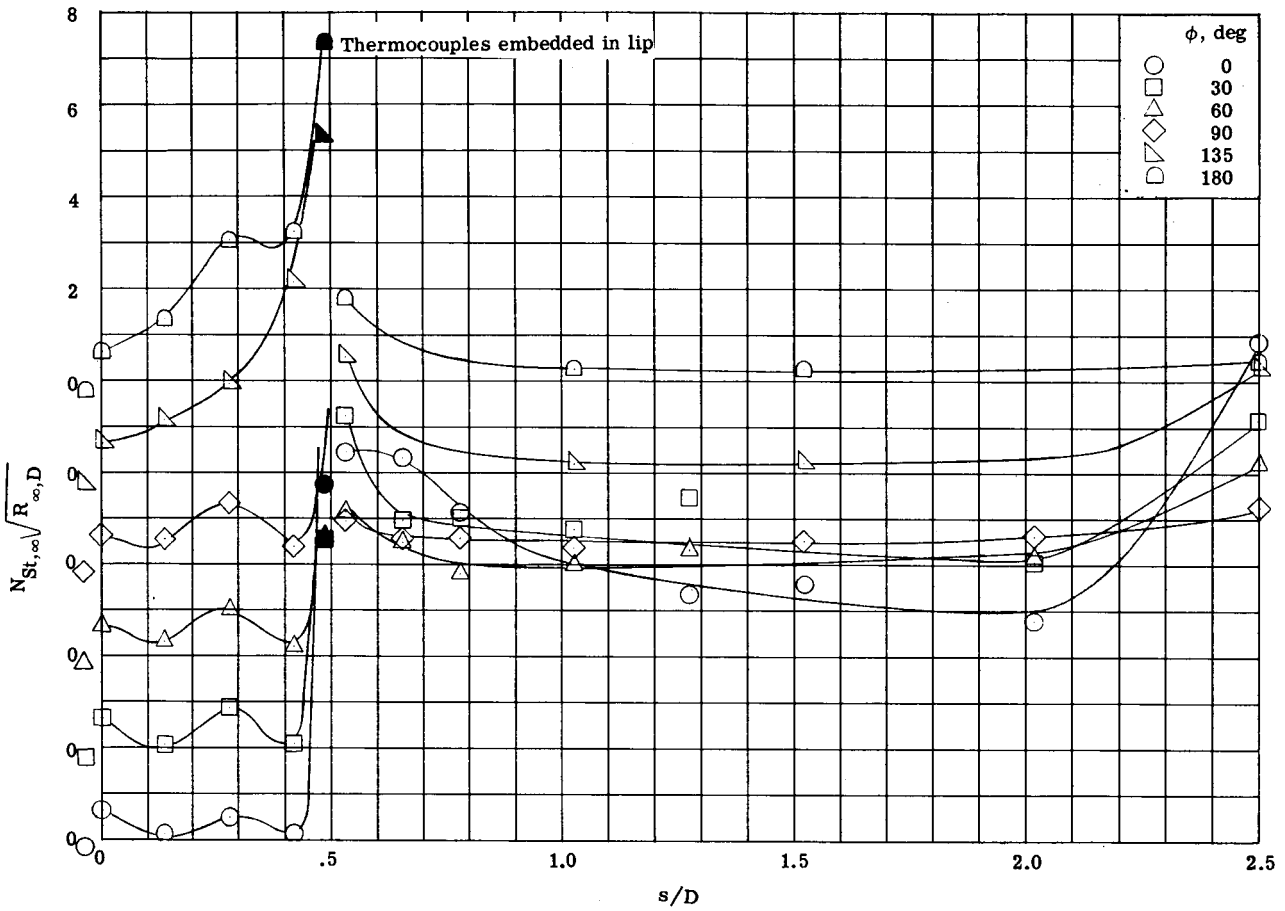

(i) $\alpha = 80.0^{0}$.

Figure 7.- Continued.

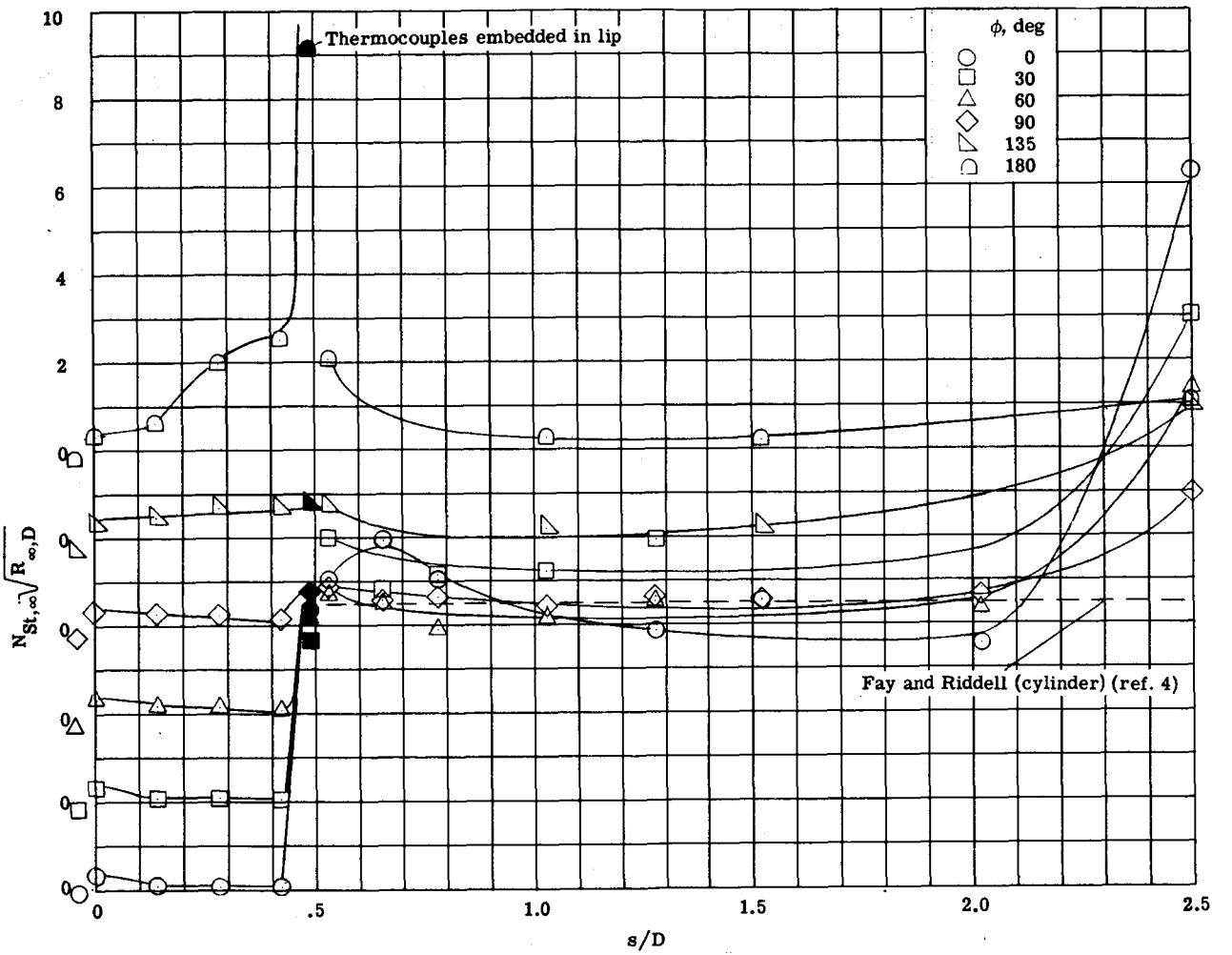

(j) $\alpha = 90.0^{\circ}$.

Figure 7.- Concluded.

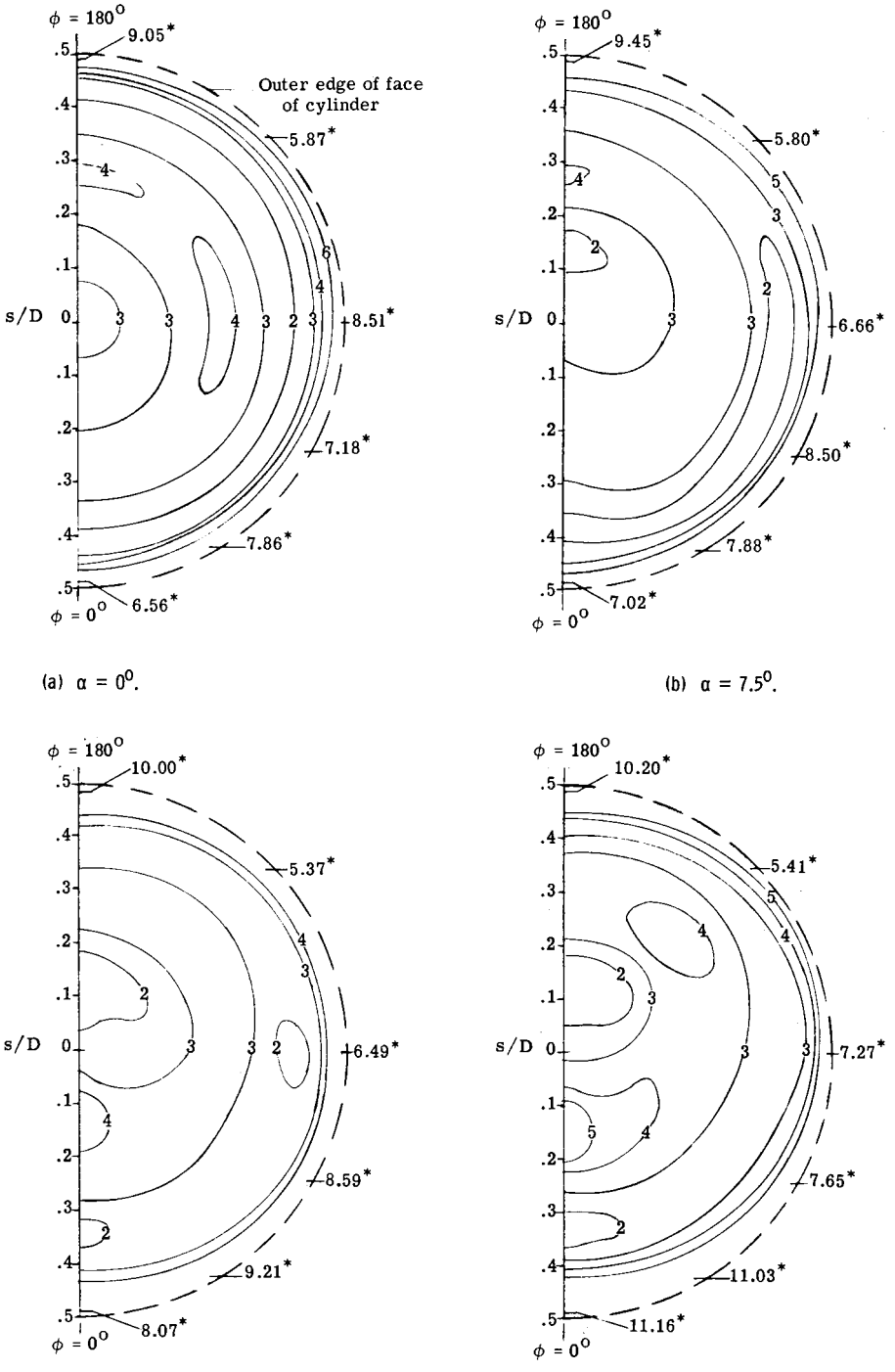

(a) $\alpha = 0^{\circ}$.

(b) $\alpha = 7.5^{\circ}$.

(c) $\alpha = 15.0^{\circ}$.

(d) $\alpha = 25.0^{\circ}$.

Figure 8.- Contour plots of heat-transfer parameter $N_{St,\infty}\sqrt{R_{\infty,D}}$ on the face of the cylinder. $R_{\infty,D} = 39.79 \times 10^4$. * (Values of heat-transfer parameter on lip of face of cylinder.)

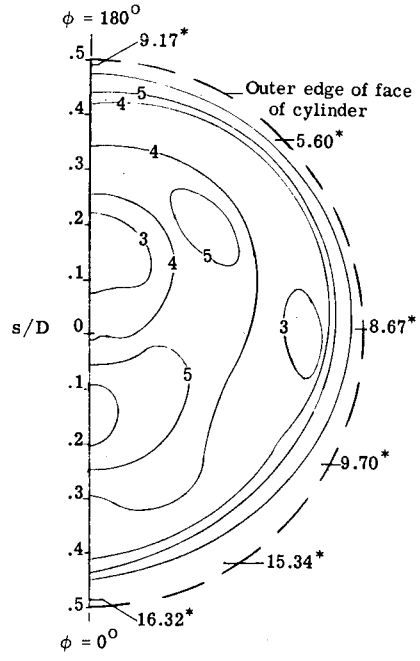

(e) $\alpha = 32.5^{\circ}$.

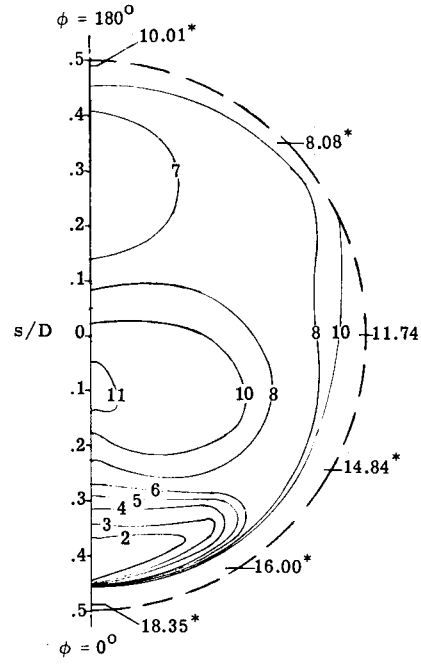

(f) $\alpha = 40.0^{\circ}$.

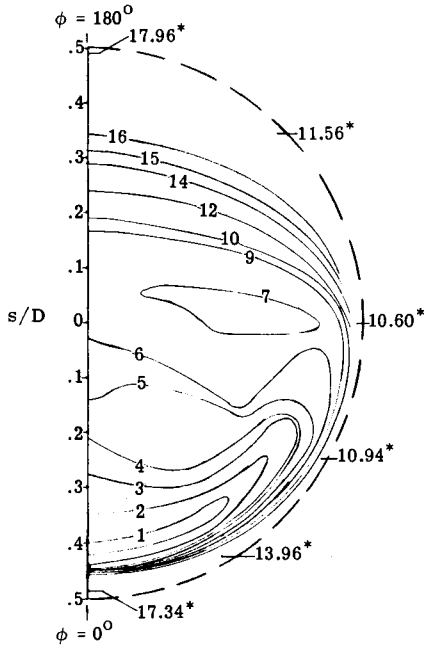

(g) $\alpha = 50.0^{\circ}$.

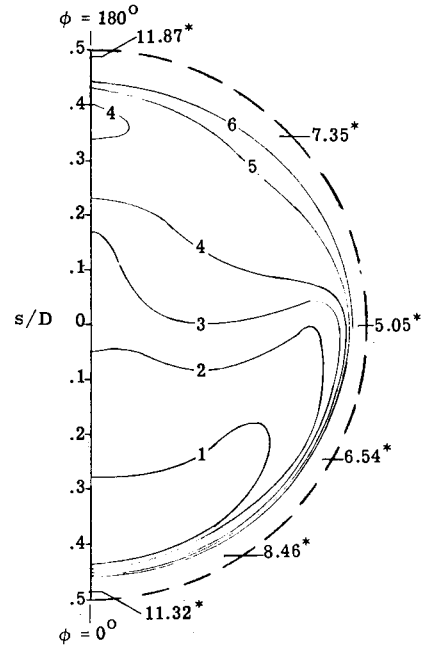

(h) $\alpha = 65.0^{\circ}$.

Figure 8.- Continued.

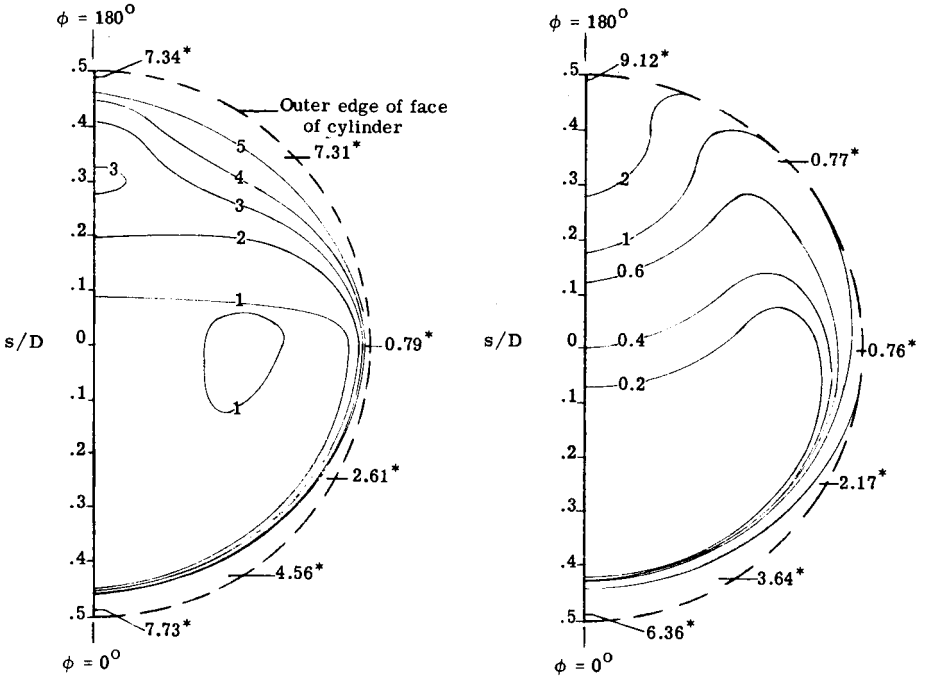

(i) α = 80.0°.

(j) α = 90.0°.

Figure 8.- Concluded.

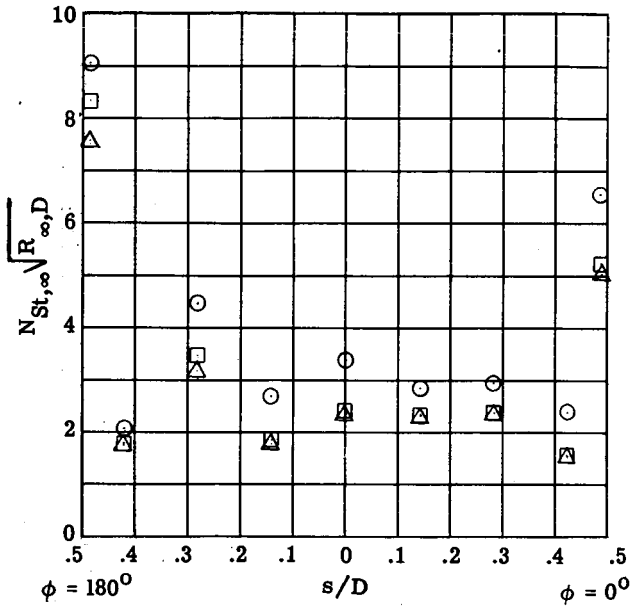

(a) $\alpha = 0^o$.

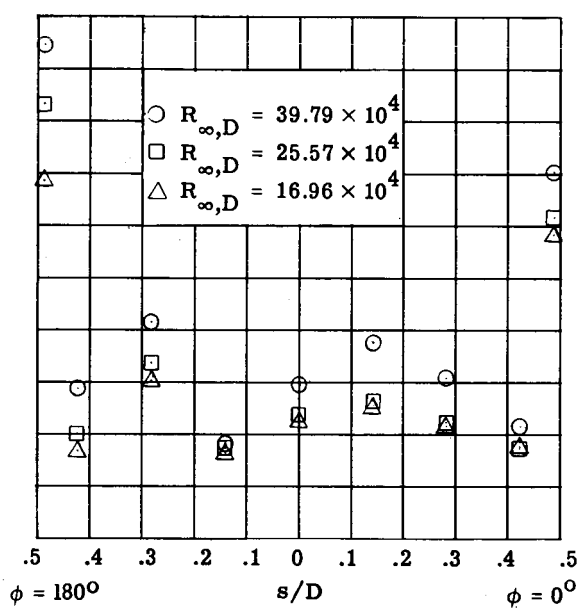

(b) $\alpha = 7.5^o$.

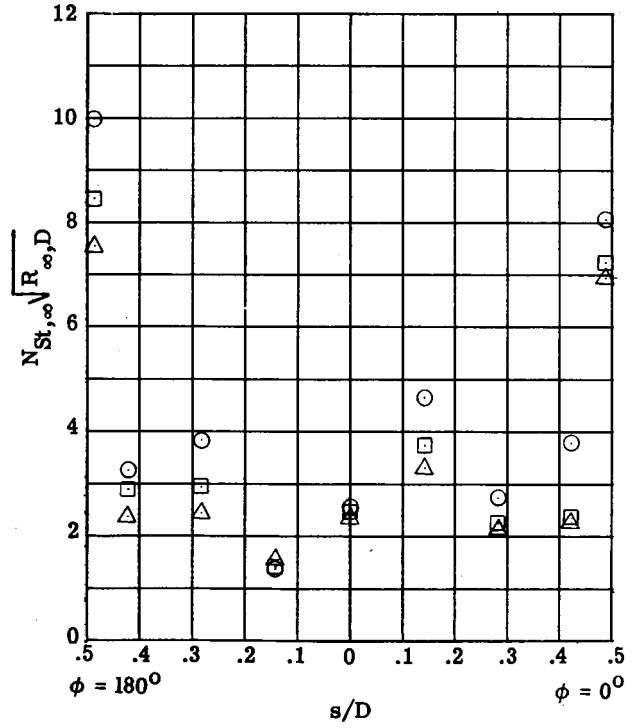

(c) $\alpha = 15.0^o$.

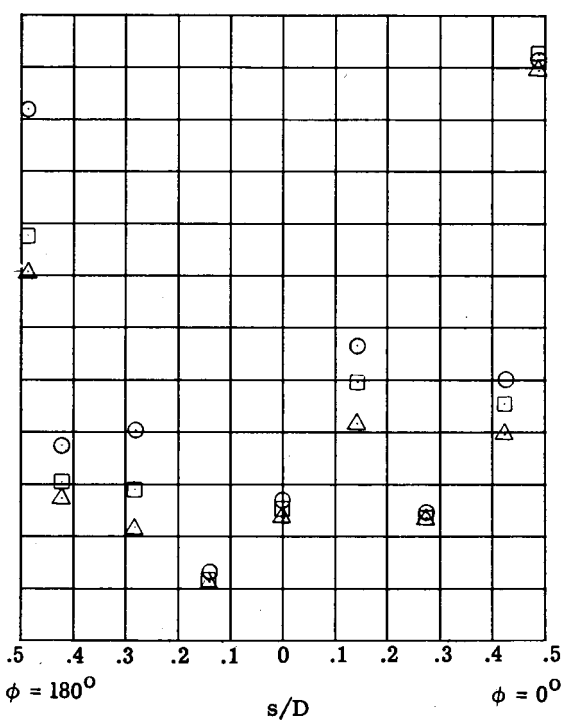

(d) $\alpha = 25.0^o$.

Figure 9.- Effect of Reynolds number on heat-transfer parameter on face of cylinder.

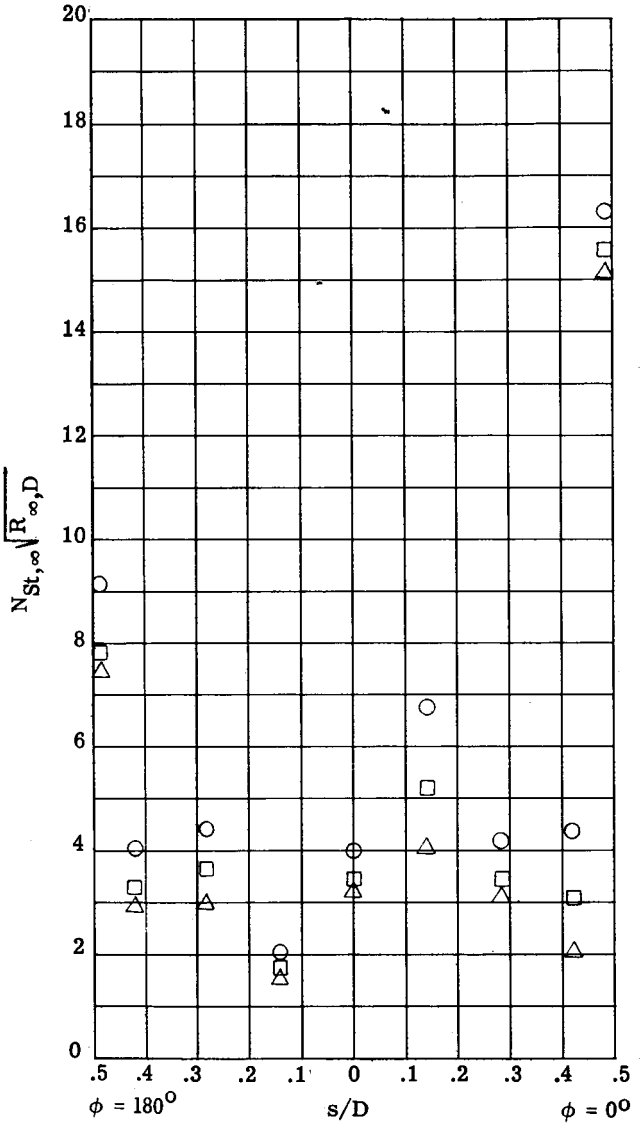

(e) $\alpha = 32.5^o$.

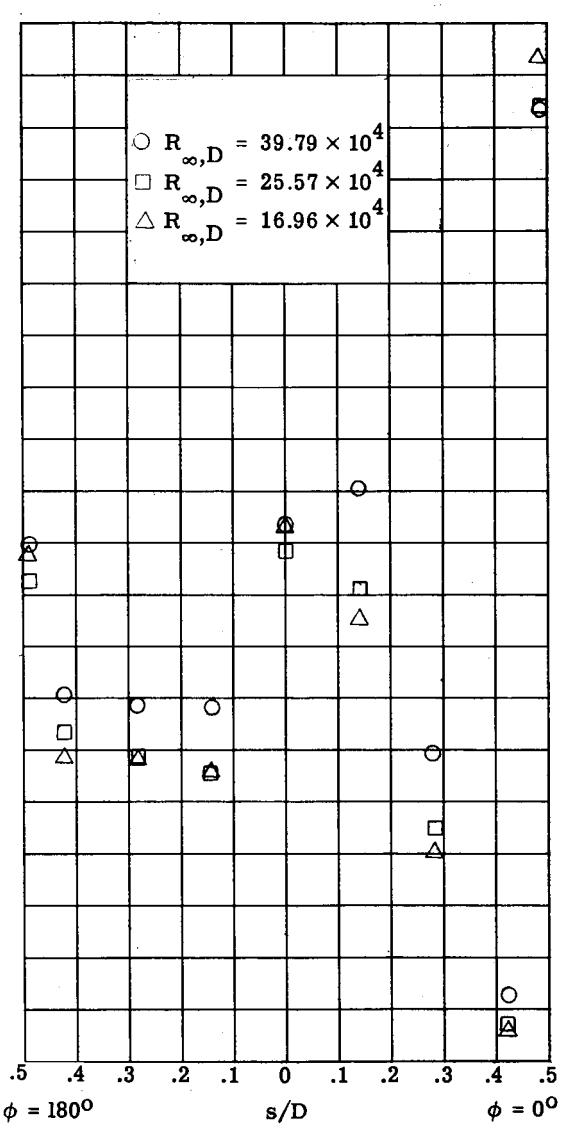

(f) $\alpha = 40.0^o$.

Figure 9.- Continued.

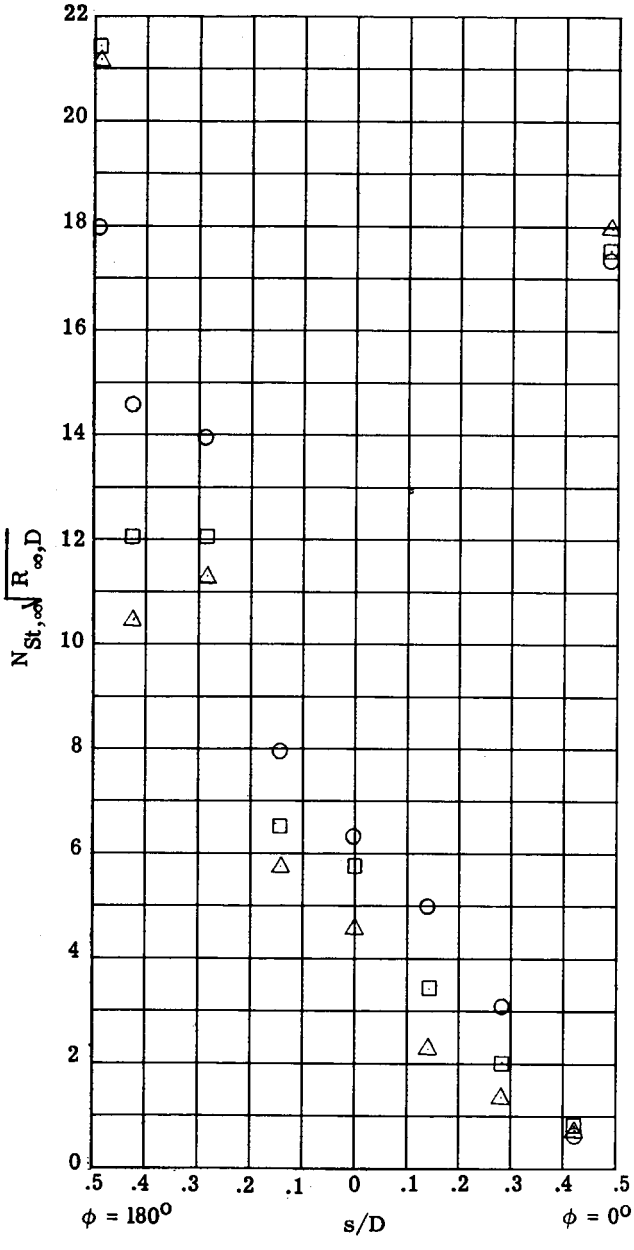

(g) $\alpha = 50.0^o$.

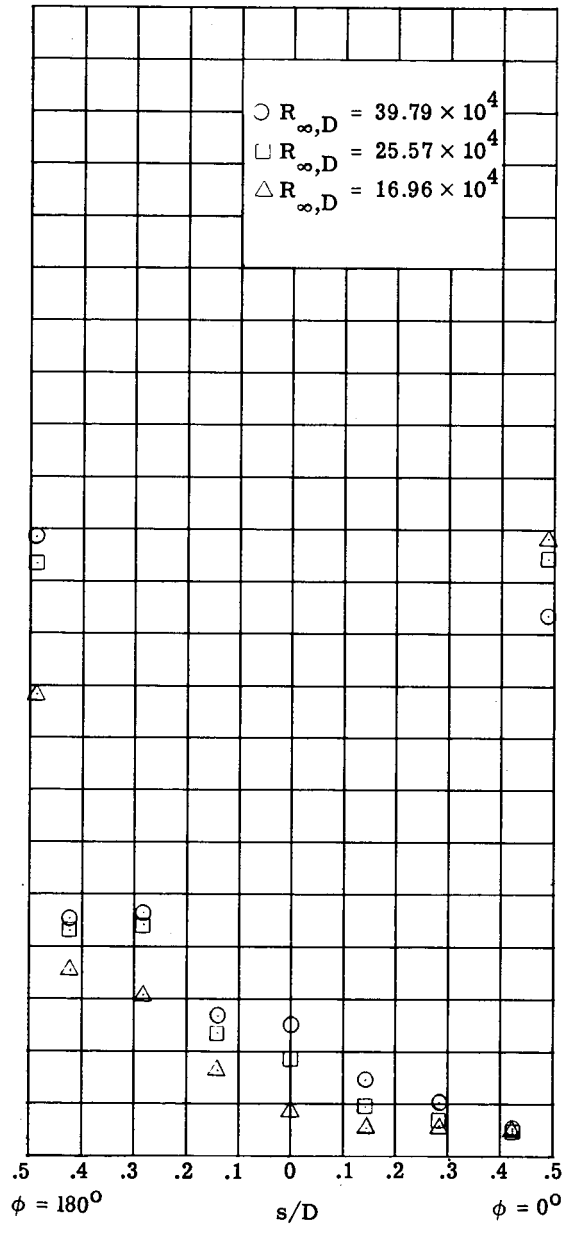

(h) $\alpha = 65.0^o$.

Figure 9.- Continued.

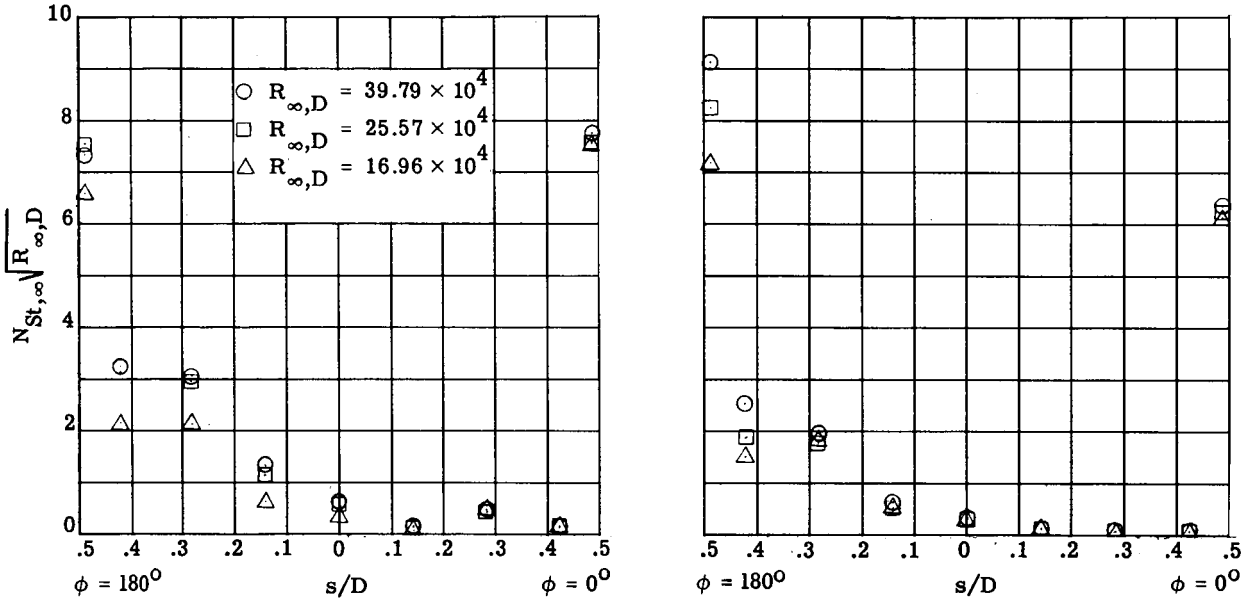

(i) $\alpha = 80.0^o$.

(j) $\alpha = 90.0^o$.

Figure 9.- Concluded.